Journal of Materials Chemistry C

PAPER

View Article Online
View Journal | View Issue

Cite this: J. Mater. Chem. C, 2015, 3, 820

Nanostructured $La_{0.7}Sr_{0.3}MnO_3$ compounds for effective electromagnetic interference shielding in the X-band frequency range

Hilal Ahmad Reshi,[a] Avanish P. Singh,[b] Shreeja Pillai,[a] Rama Shankar Yadav,[a] S. K. Dhawan[b] and Vilas Shelke*[ac]

Received 11th September 2014
Accepted 19th November 2014

DOI: 10.1039/c4tc02040e

www.rsc.org/MaterialsC

We report a detailed study on the electromagnetic interference (EMI) shielding effectiveness (SE) properties in $La_{0.7}Sr_{0.3}MnO_3$ (LSMO) nanomaterials. The samples were prepared by a solution chemistry (sol–gel) route at different sintering temperatures. The single-phase samples with grain sizes of 22 and 34 nm showed DC electrical conductivity variation from 0.65 to 13 S cm^{-1} at room temperature. The application of a high magnetic field resulted in higher conductivity values. The electrical conductivity variation with temperature could be fitted with a variable range hopping mechanism in a limited temperature range. The variation of frequency dependent electromagnetic parameters measured at room temperature within the X-band region is consistent with the electrical conductivity behavior. The complex permittivity and permeability parameters were determined in line with the Nicolson–Ross–Weir algorithm. The LSMO nanomaterial samples showed EMI shielding effectiveness values of up to 19 dB (96.3% attenuation) over the X-band frequency range, making them suitable for microwave radiation shielding in commercial and defense appliances.

Introduction

The inevitable use of several personal electronic gadgets, home appliances and commercial/industrial equipment has created electromagnetic radiation pollution. The adverse effect of electromagnetic interference (EMI) on electronic functionality and human health has triggered the search for suitable absorbing materials. The rapid development of wireless telecommunication, local area networks, radar navigation and many home appliances necessitate the improvement of electromagnetic interference shielding. EM wave absorbing materials are required to have a strong absorption over a wide range of frequencies and should be lightweight, flexible, corrosion resistant, cost effective and easy to process. A variety of nanomaterials including carbon nanotubes, graphene oxides, transition metal oxides and their composites have been studied in recent years for this purpose.[1–10] There are a number of aspects such as conducting, grounding, electrostatic discharge (ESD), *etc.* which contribute to the overall performance of the shielding materials. An extensive number of studies have been devoted to exploring highly efficient materials that attain good quality EMI radiation absorption properties. To provide an adequate solution for the EMI problem, it has been observed that materials with moderate electrical conductivity and dielectric nature can contribute to a high EMI shielding effectiveness (SE).[11–13] Materials with incipient electric and magnetic dipole moments may also be suitable candidates for electromagnetic radiation absorption.

Ferromagnetic materials are important for modern technological applications in all kinds of domestic power to high speed electronic devices.[14] Magnetic materials possess tuneable conductivity and magnetism making them promising candidates for microwave absorption materials. In particular, doped perovskite manganites have attracted widespread attention due to their unique properties, such as colossal magnetoresistance (CMR), metal–insulator transition, and spin-polarized conduction. We have studied several physical properties of these materials in the bulk form.[15–18] The rare-earth manganite with composition $La_{0.7}Sr_{0.3}MnO_3$ (LSMO) is a fascinating material as it possesses a unique combination of electrical and magnetic properties. Such compounds also show distinct features when synthesized in nanomaterial form.[19,20] The tendency of these materials to localize or delocalize charge carriers; order and reorder magnetic moments with external stimuli such as temperature, magnetic field, *etc.* motivated us to study them for electromagnetic radiation shielding. An epoxy composite of bulk LSMO has been reported to show microwave shielding with a peak reflection loss of 23 dB at 10.5 GHz.[21] Negative permittivity, an interesting feature, has been observed in LSMO

[a]Novel Materials Research Laboratory, Department of Physics, Barkatullah University, Bhopal 462026, M.P., India. E-mail: drshelke@gmail.com
[b]Polymeric and Soft Materials Section, CSIR-National Physical Laboratory, Dr K S Krishnan Road, New Delhi 440012, India
[c]Department of Materials Science and Nanoengineering, Rice University, Houston 77005, TX, USA

with variable Sr content.[22] Similarly, Zang and Cao reported microwave absorption in transition metal doped LSMO compounds.[23] In these studies, the shielding efficiency was high around a narrow frequency band. However, a material will be more suitable for device applications if the response is consistent over a wide range of frequencies. In this paper, we report the synthesis of LSMO nanoparticles through a chemical route. The crystal structure, morphologies, electrical conductivity, electromagnetic scattering parameters and EMI shielding effectiveness were examined. The pristine samples without any substitution or composite formation showed EMI shielding efficiencies (SE) of around 19 dB (96.3% attenuation) over a wide microwave frequency range (X-band).

Experimental procedure

LSMO nanopowder with nominal composition $La_{0.7}Sr_{0.3}MnO_3$ was prepared by a well known sol–gel route. Stoichiometric amounts of lanthanum(II) acetate hydrate (99.9%), strontium acetate (99.5%) and manganese(II) acetate tetrahydrate (99%) were dissolved in distilled water with acetic acid and ethylene glycol to obtain individual transparent solution precursors. These precursors were mixed dropwise at room temperature under continuous stirring. Ammonium acetate was added to enhance the homogeneity and maintain the pH around the neutral range. This mixture was heated slowly at 80 °C to evaporate the excess water and to obtain a gel. A brown-black coloured powder was formed after heating the gel at 110 °C. The powder was ground manually for two hours and calcined at 500 °C for 12 hours. The calcined mass was pressed into 12 mm diameter pellets. The pellets were divided into two batches and sintered at 600 °C (LSM6) and 800 °C (LSM8) in ambient air for 2 hours.

We used an X-ray diffractometer (D8 advanced Bruker) with CuK_α radiation ($\lambda = 1.54$ Å) to determine the phase purity and crystal structure of the samples. The X-ray diffraction patterns were analyzed by Rietveld refinement using the FULLPROF package. The DC electrical conductivity measurements were carried out by a four probe method using a commercial cryostat (Oxford Instruments Inc., UK) in the temperature range 10 K to 300 K with and without a high magnetic field. The nanostructure of the LSMO particles was observed using transmission electron microscopy (TEM). An Agilent E8362B vector network analyzer was used to explore the EMI shielding compatibility of the LSMO nanoparticles in the X-band frequency range. The powder samples were pelletized in a rectangular die with dimensions 22 × 10 mm^2 and thickness ~2 mm and loaded into a copper sample holder connected between the waveguide flanges of the network analyzer.

Results and discussion

Structural

The X-ray diffraction (XRD) patterns revealed the formation of single -phase compounds for the samples sintered at 600 (LSM6) and 800 (LSM8) °C as shown in Fig. 1a. A representative Rietveld refined graph of the LSM6 sample is shown in Fig. 1b. The Rietveld refinement confirmed an orthorhombic perovskite structure with space group *Pnma*. The structural parameters for both samples are given in Table 1. Since the chemical composition and calcination temperature were the same for both samples, they did not show any significant change in lattice parameters. Goodness of fit values below 2 illustrated a good agreement between the observed and calculated data. It also pointed out that LSMO can be synthesized by the sol–gel method even at the relatively low temperature of 600 °C. According to the phase diagram of bulk rare earth manganite the $La_{0.7}Sr_{0.3}MnO_3$ composition should show a rhombohedrally distorted (R3C) perovskite structure. However, the nanomaterial sample with the same composition shows an orthorhombic structure.[19]

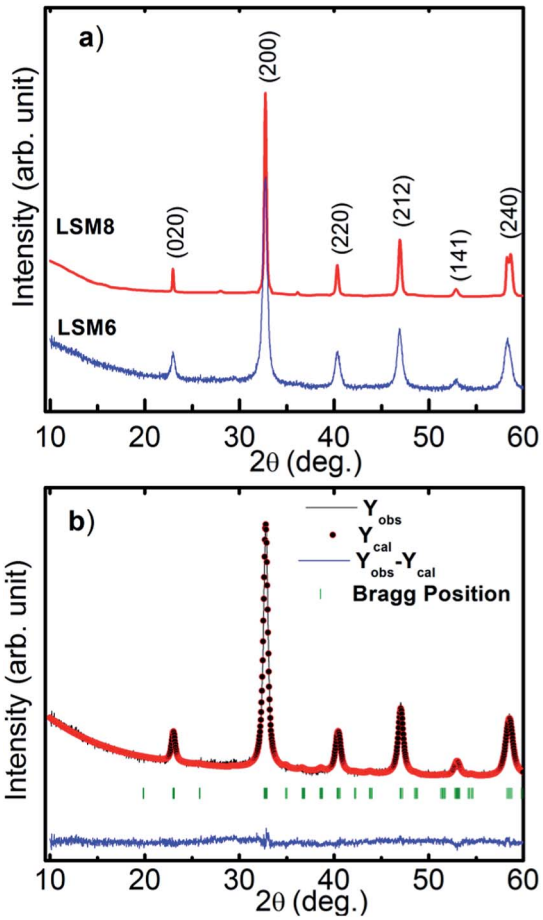

Fig. 1 X-ray diffraction patterns of (a) LSM6 and LSM8 samples and (b) representative Rietveld refined XRD pattern.

Microstructure

The grain morphology is very important to facilitate electromagnetic absorption properties because grain boundaries act as electromagnetic wave attenuation centres leading to electric/magnetic loss.[24] Fig. 2a and b are the TEM images of the LSM6 and LSM8 samples along with their selected area electron diffraction (SAED) patterns, respectively. The grain size distribution is quite narrow with distinctly dispersed

Table 1 Refined structural parameters obtained from Rietveld refinement analysis

Parameters		LSM8	LSM6
a (Å)		5.342	5.446
b (Å)		7.711	7.712
c (Å)		5.601	5.487
V (Å^3)		230.717	230.518
La^{+3}	x	0.0109	0.0148
	y	0.2500	0.2500
	z	0.0070	0.0114
Mn^{+3}	x	0.0000	0.0000
	y	0.0000	0.0000
	z	0.5000	0.5000
O_1^{-2}	x	0.4108	0.5041
	y	0.2500	0.2500
	z	−0.0731	−0.0090
O_2^{-2}	x	0.3801	0.2009
	y	−0.0192	0.0221
	z	−0.3365	0.6819
R_{wp}		6.13	4.16
R_p		5.09	5.36
R_e		13.91	13.83
R_{Bragg}		5.68	7.91
χ^2		1.57	1.54

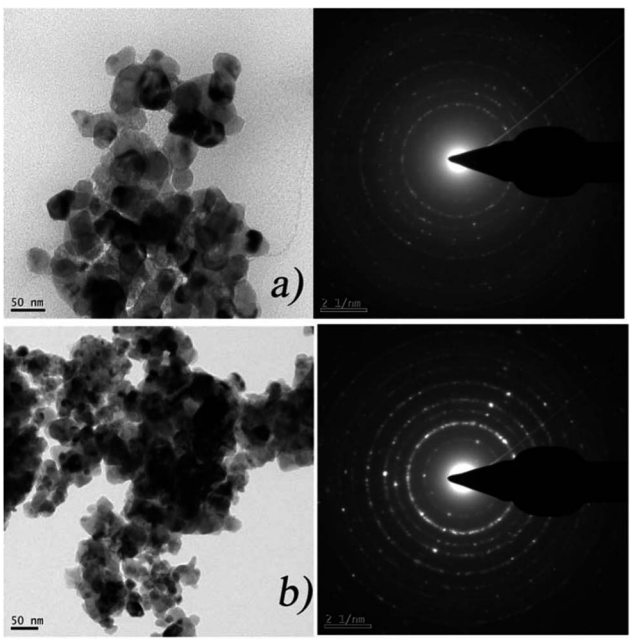

Fig. 2 Transmission electron microscopy images of (a) LSM6 and (b) LSM8 samples with SAED patterns.

nanoparticles. The average grain sizes for LSM6 and LSM8 were 22 and 34 nm, respectively. The variation in grain size from 22 to 34 nm with higher sintering temperature is relevant to the increased grain growth.

Electrical conductivity

Fig. 3a and b indicate the temperature dependent variation of DC electrical conductivity (σ) for the LSM8 and LSM6 samples,

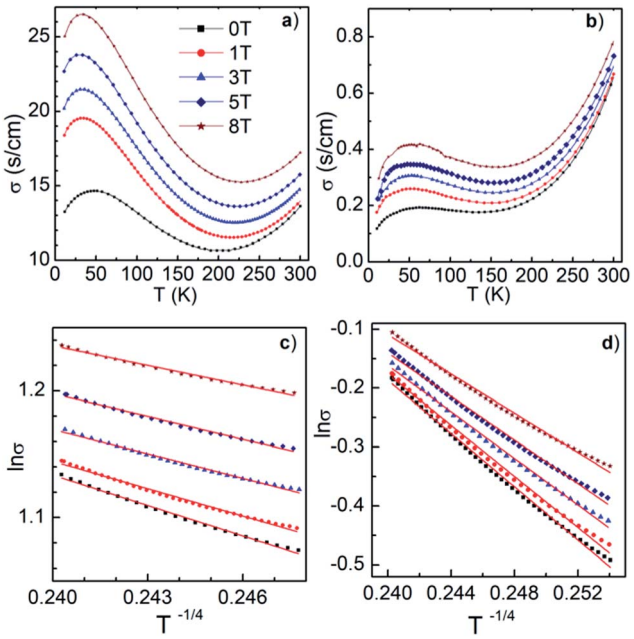

Fig. 3 Variation of DC conductivity (σ) as a function of temperature (a) σ *versus* T of the LSM8 sample, (b) σ *versus* T of the LSM6 sample, (c) (ln σ) *versus* $T^{-1/4}$ of LSM8 and (d) (ln σ) *versus* $T^{-1/4}$ of LSM6.

respectively. For sample LSM8, the conductivity values decrease with temperature in the range 300–200 K and then increase up to 50 K before showing a further decline. The transition from semiconductor to metallic behaviour at around 200 K is slightly unusual as bulk LSMO is not known to show metal–insulator (or semiconductor) transitions.[15] The finite size effect and excessive scattering of charge carriers from grain boundaries should be responsible for such behaviour. Sample LSM6 with a lower grain size showed lower conductivity values and mostly a reduction in conductivity with decreasing temperature. The zero-field conductivity value for LSM8 (13.8 S cm^{-1}) is around twenty times higher than that of LSM6 (0.63 S cm^{-1}) at room temperature. The effect of magnetic field on the conductivity behaviour in these samples is noteworthy. In both samples, conductivity values increase profoundly with an applied magnetic field over the entire temperature range. In spite of the large difference in the zero-field conductivity, both samples retained the typical characteristic of magnetoconductivity in the LSMO system. Positive magnetoconductivity (negative magnetoresistance) is observed at different magnetic fields.

According to percolation theory, electrical conductivity is determined by the ability of a material to form a conducting path. In LSM8 the larger grain size reduces the population of grain interfaces, which act as scattering centres, leading to a high conduction network. The difference between the conductivities produces a significant variation in the radiation shielding effectiveness of the material. Improvement in electrical conductivity plays a vital role in effective electromagnetic shielding.[25] The results suggest that moderate conductivity enhances the EMI shielding efficiency (SE). It has been observed that the introduction of conducting powders through chemical

doping or mixing increases the EMI SE.[26] It is important to understand the conductivity mechanism of our samples, in the near room temperature range. The response of our samples has been analyzed by the variable range hopping (VRH) transport mechanism.[27] The temperature dependent conductivity can be expressed as

$$\sigma = \sigma_0 \exp[(-T_0/T)^{1/4}] \quad (1)$$

where T_0 is the measure of the Mott characteristic temperature representing the hopping barrier and σ_0 is the conductivity at infinite temperature. Fig. 3c and d show the plots of ($\ln \sigma$) *versus* $T^{-1/4}$ for the LSM8 and LSM6 samples in the semiconducting region near room temperature. Both samples show a linear fit which indicates that VRH is an appropriate transport mechanism in this region. The relevant fitting parameters are mentioned in Table 2. Around room temperature, the conductivity is governed by the hopping of charge carriers. The effective amplitude of hopping is different in the two samples. The conceptual hypothesis of metallic droplets in a dielectric matrix can explain the size quantization effect to some extent.[27] The smaller grain sample has higher intergranular tunnelling and electrostatic barriers than the larger grain sample. Consequently, it is expected to show a lower conductivity.

Complex parameters

The frequency dependent variations of electromagnetic parameters *viz.*, complex permittivity ($\varepsilon^* = \varepsilon' - i\varepsilon''$) and complex permeability ($\mu^* = \mu' - i\mu''$), are shown in Fig. 4. More details of such conversion and analysis are available in the literature.[28,29] The measurements were carried out on a homogeneous powder sample with a density of around 3.4 gm cm^{-3}. Apparently, a filler-matrix type of composite was not used. It is seen from Fig. 4a and b that the real (ε') and imaginary (ε'') permittivity values are higher for the LSM8 sample compared to LSM6. Fig. 4c and d show the variation in the real (μ') and imaginary (μ'') parts of complex permeability, respectively. The real permeability (μ') shows a decreasing trend with intermittent peaks/dips as the frequency increases. The permittivity and permeability parameters were used to determine the dielectric and magnetic tangent loss of the samples, as shown in Fig. 4e and f, respectively. The dielectric tangent loss ($\tan \delta_e$) is higher in LSM8 than in the LSM6 sample. The magnetic tangent loss ($\tan \delta_m$) is higher in LSM8 than in the LSM6 sample at lower frequency.

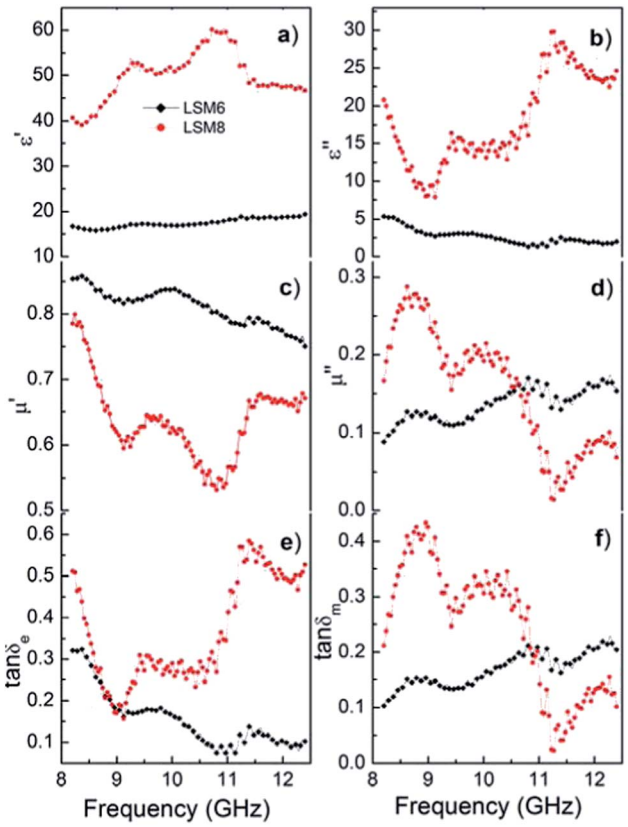

Fig. 4 Frequency dependent (a) real and (b) imaginary parts of complex permittivity; (c) real and (d) imaginary parts of complex permeability; corresponding (e) dielectric and (f) magnetic loss tangents of the LSMO samples.

The real EM parameters (ε' and μ') are directly associated with the storage ability of electric and magnetic energy while the imaginary ones (ε'' and μ'') represent the dissipation of electric and magnetic energy, respectively. The permittivity is generated from electronic, ionic, space charge, and interfacial polarization, which means that permittivity is a measure of the polarizability of a material.[30,31] The increase in permittivity can be

Table 2 Magnetic field (H) dependant DC conductivity (σ) at 300 K and 10 K along with VRH parameters for LSMO samples

Sample	H (Tesla)	σ at 300 K (S cm^{-1})	σ at 10 K (S cm^{-1})	σ_0 (S cm^{-1})	T_0 (K)
LSM8	0	13.80	13.24	3.05	4.11×10^3
	1	14.00	18.40	2.87	2.70×10^3
	3	14.76	20.15	2.71	1.69×10^3
	5	15.70	22.65	2.63	1.28×10^3
	8	17.22	25.01	2.47	0.70×10^3
LSM6	0	0.63	0.11	5.23	25.94×10^4
	1	0.67	0.17	5.02	22.05×10^4
	3	0.69	0.20	4.57	15.15×10^4
	5	0.73	0.22	4.29	11.63×10^4
	8	0.77	0.29	3.88	7.70×10^4

attributed to the increase in carrier concentration and conductivity.[32] The complex fluctuation observed in the permittivity of the LSM8 sample over the measured frequency range suggests a resonance behavior that is expected in conductive materials as a consequence of the skin effect.[33,34] This behavior could also be related to electron hopping between Mn^{+3}–O–Mn^{+4} ions at the applied EM wave frequency.[35,36] In comparison with other materials,[37–41] both the real and imaginary parts of the LSM6 and LSM8 samples are high, indicating dielectric storage and loss of electromagnetic waves. The increase of both the real and imaginary parts of the dielectric permittivity contributes towards enhancement of the total shielding efficiency. The dielectric loss mechanism includes complex phenomena such as natural resonance loss, dielectric relaxation loss, conduction loss, electronic polarization and its relaxation *etc.*[42–44] Moreover, the dielectric loss is improved by polaron hopping and bound charges which restrict the mobility and account for the strong polarization in the material.[45,46] Similarly, the wave-like nature of permeability is indicative of magnetic resonance. The appearance of clear peaks in the imaginary permeability (μ'') also implies a stronger resonance in LSM8 than in the LSM6 sample.[47] The increase in μ'' of the LSM6 sample with frequency is caused by the time lag of the magnetization vector behind the magnetic field vector. The change in the magnetization vector is generally brought about by the rotation of magnetization. These motions lag behind the change in the magnetic field and contribute to the magnetic loss.[45] The enhancement of the number of atoms with dangling bonds and surface area leads to the interface polarization due to the accumulation of charges at the interface. This plays a significant role in the microwave absorption.[47,48] The observed dielectric tangent loss is above 0.1 throughout the measured frequency range, revealing that dielectric loss occurs over a wide range. The magnetic tangent loss ($\tan \delta_m$) rises gradually over the whole frequency range for LSM6 whereas it fluctuates for LSM8 and shows a better value than LSM6 of below 10.6 GHz. This illustrates that the LSM8 sample exhibits more dielectric loss at higher frequency and more magnetic loss at lower frequency compared to the LSM6 sample.

EMI shielding effectiveness

The EMI shielding effectiveness (SE) of a material is expressed in terms of the ratio of the incident and transmitted energy and can be represented mathematically on a logarithmic scale, given by

$$\begin{aligned} SE_T\ (dB) &= -10 \log\{P_T/P_I\} = -10 \log\{E_T/E_I\} \\ &= -10 \log\{H_T/H_I\} \end{aligned} \quad (2)$$

where P_I (E_I and H_I) and P_T (E_T and H_T) are the power (electric and magnetic field) of incident and transmitted electromagnetic waves, respectively. The total shielding effectiveness (SE_T) is a contribution of three components, *viz.* absorption (SE_A), reflection (SE_R) and multiple internal reflection (SE_M). The reflection, (R) transmission (T) and absorption (A) components were obtained through the measurement of scattering parameters $S11$ (or $S22$) and $S21$ (or $S12$) of a two port network analyzer, where $R = |S11|^2$ and $T = |S21|^2$ and $A = 1 - |S11|^2 - |S21|^2$. The total shielding effectiveness (SE_T) of the samples is given by

$$SE_T = SE_R + SE_A + SE_M$$

$$SE_R = -10 \log(1 - R),\ SE_A = -10 \log(T/1 - R)$$

$$\text{and } SE_M = -20 \log(1 - 10^{-SE_A/10}) \quad (3)$$

The multiple reflection term (SE_M) can be ignored in cases where SE_T > 10 dB, or if the shield is thicker than the skin depth.[49,50] The multiple reflections term is considered for large surface areas, as in porous or foam materials, and is not significant in the present study. The primary mechanism for EMI shielding is reflection for which the shield possesses mobile charge carriers that can interact with electromagnetic waves. The shield needs electrically moderate conductivity of around 10^{-3} to 1 S m^{-1}.[51,52] The strong and effective secondary mechanism is absorption resulting from the interaction of electric/magnetic dipoles with electromagnetic radiation. Fig. 5 shows the frequency dependence of EMI shielding effectiveness along with the total attenuation values for both samples. The

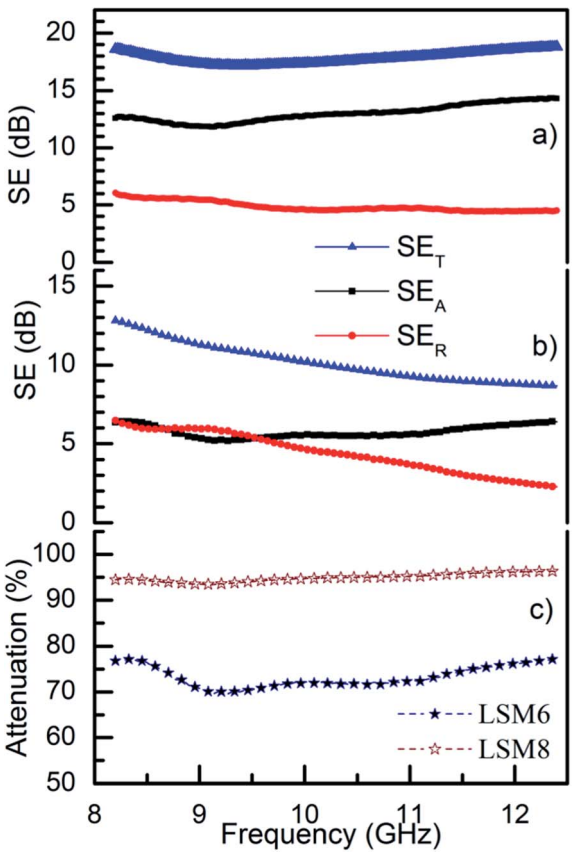

Fig. 5 Frequency dependent electromagnetic shielding effectiveness of (a) LSM8, (b) LSM6 and (c) attenuation values for both of the compounds.

experimental measurements reveal that shielding effectiveness due to absorption (SE_A) and reflection (SE_R) varies from 12.3 dB to 14.1 dB and 6 dB to 4.3 dB in LSM8, whereas it varies from 5.5 dB to 7 dB and 6.5 dB to 2.2 dB in LSM6, respectively. The maximum values of the total shielding effectiveness (SE_T) achieved for the LSM8 and LSM6 samples are 19 dB and 13 dB, which correspond to an attenuation of 96.3% and 77.4%, respectively. In both samples, SE_R decreases and SE_A increases with the increase in frequency. Therefore, the total shielding effectiveness remains almost constant in the entire frequency range. A uniform shielding over a wide range of frequency is the prominent feature of these samples. By increasing the sintering temperature, the conductivity also increases and SE_T increases from 12.9 to 19 dB as shown in Fig. 5. These results, associated with the dielectric and magnetic parameters in Fig. 4, indicate that improvement of the magnetic and dielectric properties of the LSMO nanostructures has a significant effect on the improvement of the microwave range shielding efficiency.

Theoretical understanding of the intricate mechanism of EMI shielding is beyond the scope of the present study. A detailed analysis based on forward/backward propagation matrices inserted with generic algorithms and effective theoretical design for nanoparticle fillers has been reported by Micheli *et al.*[53,54] Qualitatively, the real part of permittivity is strongly related to electric charge accumulation due to interfacial polarization effects and the imaginary part is due to loss effects.[55] The conduction or quantum mechanical tunnelling currents contribute to the losses. At high frequency (f), electromagnetic radiation penetrates only at the near surface region of the sample. The electric field of a plane wave drops exponentially with increasing depth into the material. The depth at which the field drops to $1/e$ of the incident value is called the skin depth (δ). The AC conductivity (σ_{AC}) and skin depth (δ) are related to the imaginary permittivity (ε'') and real permeability (μ') as $\sigma_{AC} = 2\pi f\varepsilon_0\varepsilon''$ and $\delta = (2/\sigma_{AC}2\pi f\mu')^{1/2}$. In order to find out the effect of conductivity on the shielding parameters, we plotted σ_{AC} against the measured frequency range (Fig. 6a). Usually, the shielding effectiveness can be enhanced by increasing the metal layer or the conductivity.[56] The conductivity shows an oscillatory behaviour for both of the samples and is higher for LSM8 than for the LSM6 sample. The variation of skin depth δ with frequency is shown in Fig. 6b. The skin depth increases with frequency initially for both samples, which demonstrates a lack of surface conduction. However, in LSM8, the skin depth decreases with an increase in frequency, which reveals that surface conduction may improve at higher frequencies. Conductivity and magnetic permeability of the material play a significant role in reducing or enhancing the skin depth. The maximum skin depth of LSM6 is around 6 mm while that of LSM8 is 3.4 mm. Samples showing optimum values of conductivity and magnetization are desirable for exhibiting good microwave shielding applications.[57]

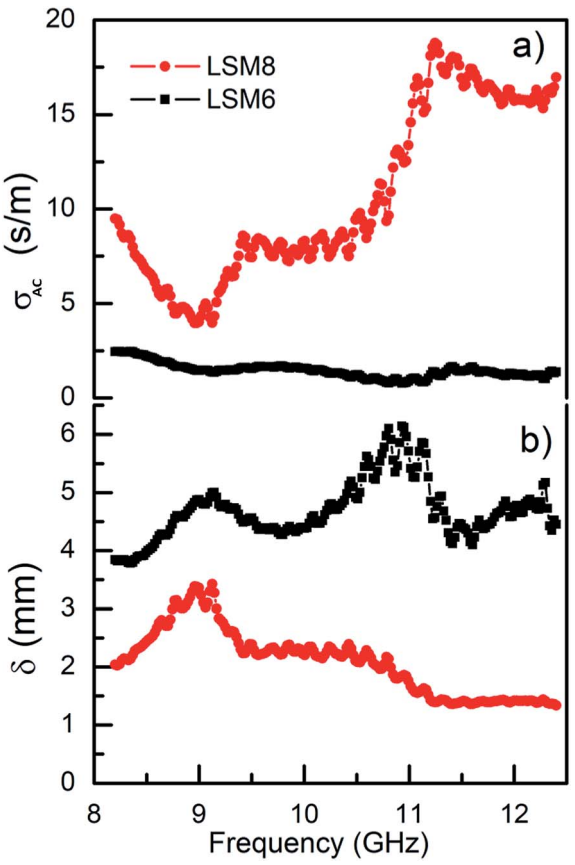

Fig. 6 The frequency dependent variation of (a) AC conductivity (σ_{AC}) and (b) skin depth (δ) for the LSM8 and LSM6 samples.

Conclusions

We synthesized LSMO nanoparticles by a solution chemistry (sol–gel) route with grain sizes of 22 and 34 nm. The nanomaterial samples showed phase pure compounds with orthorhombic *Pnma* crystal structures. The samples showed metal–insulator transition and magnetoconductivity effects. The semiconducting region follows a variable range hopping transport mechanism. The variation of permittivity suggests a resonance behavior observed in conducting materials while the permeability manifests the magnetic energy storage and loss. Total shielding effectiveness values of 19 (96.3% attenuation) and 13 dB (77.4% attenuation) have been achieved in the two samples over the X-band frequency range. The high value of shielding effectiveness is mostly dominated by absorption rather than reflection. The occurrence of significant shielding effectiveness illustrated that nano LSMO is a promising oxide material for EMI shielding in the microwave frequency range.

Acknowledgements

This work is financially supported by M. P. Council of Science and Technology, Bhopal and the University Grants Commission, New Delhi. Part of the work was performed at UGC-DAE Consortium for Scientific Research, Indore, India. The authors are thankful to Dr Mukul Gupta and Dr Rajiv Rawat for providing experimental facilities.

Notes and references

1 B. Shen, W. Zhai and W. Zheng, *Adv. Funct. Mater.*, 2014, **24**, 4542.
2 N. Youse, X. Sun, X. Lin, X. Shen, J. Jia, B. Zhang, B. Tang, M. Chan and J. K. Kim, *Adv. Mater.*, 2014, **26**, 5480.
3 B. Wen, M. Cao, M. Lu, W. Cao, H. Shi, J. Liu, X. Wang, H. Jin, X. Fang, W. Wang and J. Yuan, *Adv. Mater.*, 2014, **26**, 3484.
4 N. Li, Y. Huang, F. Du, X. He, X. Lin, H. Gao, Y. Ma, F. Li, Y. Chen and C. Eklund, *Nano Lett.*, 2006, **6**, 1141.
5 J. Zhu, S. Wei, L. Zhang, Y. Mao, J. Ryu, N. Haldolaarachchiqe, D. P. Young and Z. Guo, *J. Mater. Chem.*, 2011, **21**, 3952.
6 X. Li, L. Zhang and X. Yin, *J. Am. Ceram. Soc.*, 2012, **95**, 1038.
7 A. P. Singh, M. Mishra, A. Chandra and S. K. Dhawan, *Nanotechnology*, 2011, **22**, 465701.
8 A. P. Singh, M. Mishra, P. Sambyal, B. K. Gupta, B. P. Singh, A. Chandra and S. K. Dhawan, *J. Mater. Chem. A*, 2014, **2**, 3581.
9 Y. J. Chen, G. Xiao, T. S. Wang, Q. Y. Ouyang, L. H. Qi, Y. Ma, P. Gao, C. L. Zhu, M. S. Cao and H. B. Jin, *J. Phys. Chem. C*, 2011, **115**, 13603.
10 G. Tong, W. Wu, Q. Hua, Y. Miao, J. Guan and H. Qian, *J. Alloys Compd.*, 2011, **509**, 451.
11 M. Loeblein, R. Yingjie Tay, S. Hon Tsang, W. Beng Ng, E. Hang and T. Teo, *Small*, 2014, **10**, 2992.
12 H. M. Kim, K. Kim, C. Y. Lee, J. Joo, S. J. Cho, H. S. Yoon, D. A. Pejakovic, J. W. Yoo and A. J. Epstein, *Appl. Phys. Lett.*, 2004, **84**, 589.
13 R. Che, L. M. Peng, X. Duan, Q. Chen and X. Liang, *Adv. Mater.*, 2004, **16**, 401.
14 N. A. Spaldin, *Magnetic materials, Fundamentals and applications*, Cambridge University press, New York, 2011, p. 270.
15 V. Shelke, A. Das, I. Dhiman, R. Yadav, S. Khatarkar, A. Anshul and R. K. Singh, *J. Phys.: Condens. Matter*, 2008, **20**, 395218.
16 V. Shelke, S. Khatarkar, R. Yadav, A. Anshul and R. K. Singh, *J. Magn. Magn. Mater.*, 2010, **322**, 1224.
17 R. Yadav, A. Anshul and V. Shelke, *J. Mater. Sci.: Mater. Electron.*, 2011, **22**, 1173.
18 R. Singh, D. Bhuwal, R. Yadav, S. Khatarkar and V. Shelke, *IEEE Trans. Magn.*, 2012, **48**, 1155.
19 H. A. Reshi, S. Pillai, D. Bhuwal and V. Shelke, *J. Nanosci. Nanotechnol.*, 2013, **13**, 4608.
20 K. Das, R. Rawat, B. Satpati and I. Das, *Appl. Phys. Lett.*, 2013, **103**, 202406.
21 R. B. Yang, C. Y. Tsay, W. F. Liang and C. K. Lin, *J. Appl. Phys.*, 2010, **107**, 09A523.
22 K. L. Yan, R. H. Fan, Z. C. Shi, M. Chen, L. Qian, Y. L. Wei, K. Sun and J. Li, *J. Mater. Chem. C*, 2014, **2**, 1028.
23 S. Zhang and Q. Cao, *J. Mater. Sci. Eng. B*, 2012, **177**, 678.
24 M. Faisal and S. Khasim, *J. Mater. Sci.: Mater. Electron.*, 2013, **24**, 2202.
25 S. W. Kim, J. H. Li, J. Kim and H. W. Lee, *J. Am. Ceram. Soc.*, 2004, **87**, 2213.
26 J. Joo and C. Y. Lee, *J. Appl. Phys.*, 2000, **88**, 513.
27 Y. K. Vekilov and Y. M. Mukovskii, *Solid State Commun.*, 2012, **152**, 1139.
28 A. M. Nicolson and G. F. Ross, *IEEE Trans. Instrum. Meas.*, 1970, **19**, 377.
29 S. H. Park, P. T. Theilmann, M. Asbeck and P. R. Bandaru, *IEEE Trans. Nanotechnol.*, 2010, **9**, 464.
30 X. S. Feng, C. H. Ye, T. Xie, Z. Y. Wang, J. W. Zhao and L. D. Zhang, *Appl. Phys. Lett.*, 2006, **88**, 013101.
31 L. Deng, L. Ding, K. Zhou, S. Huang, Z. Hu and B. Yang, *J. Magn. Magn. Mater.*, 2011, **323**, 1895.
32 L. Kong, X. Yin, Q. Li, F. Ye, Y. Liu, G. Duo and X. Yuan, *J. Am. Ceram. Soc.*, 2013, **96**, 221.
33 D. A. Durkee, H. B. Eitouni, E. D. Gomez, M. W. Ellsworth, A. T. Bell and N. P. Balsara, *Adv. Mater.*, 2005, **17**, 2003.
34 Z. Liu, G. Bai, Y. Huang, Y. Ma, F. Du, F. Li, T. Guo and Y. Chen, *Carbon*, 2007, **45**, 821.
35 R. P. Pawar, R. N. Jadhav and V. Puri, *Electron. Mater. Lett.*, 2012, **8**, 32.
36 S. M. Abbas, R. Chatterjee, A. K. Dixit, A. V. Kumar and T. C. Goel, *J. Appl. Phys.*, 2007, **101**, 074105.
37 Y. L. Cheng, J. M. Dai, X. B. Zhu, D. J. Wu, Z. R. Yang and Y. P. Sun, *Nanoscale Res. Lett.*, 2009, **4**, 1153.
38 A. Cao, Z. Liu, S. Chu, M. Wu, Z. Ye, Z. Cai, Y. Chang, S. Wang, Q. Gong and Y. Liu, *Adv. Mater.*, 2010, **22**, 103.
39 Z. S. Wu, W. Ren, L. Wen, L. Gao, J. Zhao, Z. Chen, G. Zhao, F. Li and H. M. Cheng, *ACS Nano*, 2010, **4**, 3187.
40 Y. J. Chen, F. Zhang, G. G. Zhao, X. Y. Fang, H. B. Jin, P. Gao, C. L. Zhu, M. S. Cao and G. Xiao, *J. Phys. Chem. C*, 2010, **114**, 9239.
41 G. Zhou, D. W. Wang, F. Li, L. Zhang, N. Li, Z. S. Wu, L. Wen, G. Q. Lu and H. M. Cheng, *Chem. Mater.*, 2010, **22**, 5306.
42 G. Tong, W. Wu, Q. Hua, Y. Miao, J. Guan and H. Qian, *J. Alloys Compd.*, 2011, **509**, 451.
43 G. Tong, J. Ma, W. Wu, Q. Hua, R. Qiao and H. Qian, *J. Mater. Res.*, 2011, **26**, 682.
44 J. Huo, L. Wang and H. Yu, *J. Mater. Sci.*, 2009, **44**, 3917.
45 A. Ohlan, K. Singh, A. Chandra, V. N. Singh and S. K. Dhawan, *J. Appl. Phys.*, 2009, **106**, 044305.
46 S. W. Phang, T. Hino, M. H. Abdullah and N. Kuramoto, *Mater. Chem. Phys.*, 2007, **104**, 327.
47 X. F. Zhang, X. L. Dong, H. Huang, Y. Y. Liu, W. N. Wang, X. G. Zhu, B. Lv, J. P. Lei and C. G. Lee, *Appl. Phys. Lett.*, 2006, **89**, 053115.
48 C. L. Zhu, M. L. Zhang, Y. L. Qiao, G. Xiao, F. Zhang and Y. J. Chen, *J. Phys. Chem. C*, 2010, **114**, 16229.
49 N. C. Das, D. Khastgir, T. K. Chaki and A. Chakraborty, *Composites, Part A*, 2000, **31**, 1069.
50 M. H. Al-Saleh and U. Sundararaj, *J. Phys. D: Appl. Phys.*, 2013, **46**, 035304.
51 P. Saini, V. Choudhary, B. P. Singh, R. B. Mathur and S. K. Dhawan, *Synth. Met.*, 2011, **161**, 1522.
52 W. H. Otto, *Electromagnetic compatibility engineering*, John Wiley & Sons, New Jersey, 2009.

53 D. Micheli, R. Pastore, C. Apollo, M. Marchetti, G. Gradoni, V. M. Primiani and F. Moglie, *IEEE Trans. Microwave Theory Tech.*, 2011, **59**, 2633.
54 D. Micheli, C. Apollo, R. Pastore, D. Barbera, R. B. Morles, M. Marchetti, V. M. Primiani and F. Moglie, *IEEE Trans. Electromagn. Compat.*, 2012, **54**, 60.
55 D. Micheli, R. Pastore, A. Vricella, R. B. Morles, M. Marchetti, A. Delfini, F. Moglie and V. M. Primiani, *J. Mater. Sci. Eng. B*, 2014, **188**, 119.
56 S. Lucyszyn and Y. Zhou, *Prog. Electromagn. Res.*, 2010, **103**, 17.
57 A. P. Singh, P. Garg, F. Alam, K. Singh, R. B. Mathur, R. P. Tandon, A. Chandra and S. K. Dhawan, *Carbon*, 2012, **50**, 3868.